Electrical properties and structural transition of $Ge_2Sb_2Te_5$ adjusted by rare-earth element Gd for nonvolatile phase-change memory

Yongjin Chen, Nianke Chen, Bin Chen, Qing Zhang, Xianbin Li, Qingsong Deng, Bin Zhang, Shengbai Zhang, Ze Zhang, and Xiaodong Han

Citation: Journal of Applied Physics **124**, 145107 (2018); doi: 10.1063/1.5040988
View online: https://doi.org/10.1063/1.5040988
View Table of Contents: http://aip.scitation.org/toc/jap/124/14
Published by the American Institute of Physics

Electrical properties and structural transition of $Ge_2Sb_2Te_5$ adjusted by rare-earth element *Gd* for nonvolatile phase-change memory

Yongjin Chen,[1] Nianke Chen,[2] Bin Chen,[1] Qing Zhang,[1] Xianbin Li,[2,4,a)] Qingsong Deng,[1] Bin Zhang,[3,a)] Shengbai Zhang,[4] Ze Zhang,[1,5] and Xiaodong Han[1,a)]

[1]*Beijing Key Laboratory and Institute of Microstructure and Property of Advanced Materials, Beijing University of Technology, Beijing 100124, China*

[2]*State Key Laboratory on Integrated Optoelectronics, College of Electronic Science and Engineering, Jilin University, Changchun 130012, China*

[3]*Analytical and Testing Center, Chongqing University, Chongqing 401331, China*

[4]*Department of Physics, Applied Physics, and Astronomy, Rensselaer Polytechnic Institute, Troy, New York 12180, USA*

[5]*Center of Electron Microscopy and State Key Laboratory of Silicon Materials, Department of Materials Science and Engineering, Zhejiang University, Hangzhou 310027, China*

(Received 22 May 2018; accepted 15 September 2018; published online 12 October 2018)

Phase change memory has been considered as the next generation in non-volatile electronic data storage. The property modulation of such materials by the doping of rare-earth elements has drawn a lot of attention, which motivates us to search for the optimal dopants and reveal the underlying mechanisms. Here, we investigate the role of *Gd* as a dopant in $Ge_2Sb_2Te_5$, which exhibits higher crystalline resistance and better thermal stability and antioxidant capacity than the undoped counterpart. Moreover, *Gd* dopants suppress both the processes of phase transition and grain growth. The crystalline structure remains unchanged with *Gd* dopants and vacancies are randomly distributed. Furthermore, the bonding mechanism was theoretically investigated. In the amorphous state, *Gd* atoms modify the local structures around *Ge*, *Sb*, and *Te* atoms. The large coordination number of *Gd* and the "*Gd–Te* distorted pentagonal bipyramidal-like" structure can be attributed to the good thermal stability. These microscopic findings figure out some of the key issues about the bonding mechanism, electrical properties, and crystallization behaviors of *Gd* doped phase change memory materials, which could be useful for storage devices. *Published by AIP Publishing.*

https://doi.org/10.1063/1.5040988

I. INTRODUCTION

Phase-change memory materials (PCMs) have drawn significant attention for non-volatile optical and electronic data storage due to large optical or electrical contrast between different phases with rapid and reversible switching.[1,2] These unique properties also render PCMs suitable for brain-inspired computing, flexible displays, and logic devices.[3–5] In the PCMs, the quasi-binary $GeTe$-Sb_2Te_3 alloys, e.g., $Ge_2Sb_2Te_5$ (*GST*), are superior to other chalcogenide alloys in many aspects, but there still remains some room for improving their performances. Considerable efforts have been devoted to improve the thermal stability and crystallization speed using the element doping techniques.[6–15]

The modulation of the PCM properties via the doping of rare-earth element has drawn much attention. Very recently, Rao *et al.* found that $Sc_{0.2}Sb_2Te_3$ compound can boost the writing speed up to hundreds of picoseconds.[16] *Ce* doped $Ge_2Sb_2Te_5$ and *Sm* doped $Sn_{15}Sb_{85}$ films have been reported to improve the crystallization temperature and data retention ability.[10,17] *Ab initio calculations* show that as a promising dopant for Sb_2Te_3-based phase change memory, yttrium (*Y*) may improve amorphous thermal stability.[18,19] Although these experimental and theoretical results have shown the influence of some rare-earth elements on PCMs, the potential applications and their physical nature motivate us to further search for the optimal rare-earth dopants and uncover the underlying mechanisms in more detail.

Crystallization speed, non-volatile feature, resistivity contrast, and power consumption are indeed the crucial indicators for PCMs, wherein *Sc* seems to be the optimal dopant so far.[16] On the other hand, avoiding phase separation, increasing the electrical resistivity of crystalline state, and improving the thermal stability of amorphous state would also be other design rules to discover an optimal dopant. If the crystal structure after doping remains unchanged, it may show a tendency of phase-separation suppression and higher cyclability. Compared to the elements in *GST*, rare-earth element *Gd* has smaller electronegativity [(*Gd* (1.20); *Ge* (2.01); *Sb* (2.05); and *Te* (2.10)] but larger atom size [atomic radius: $r_{Gd} = 0.180$ nm; $r_{Ge} = 0.125$ nm; $r_{Sb} = 0.145$ nm; $r_{Te} = 0.140$ nm]. Moreover, the binary compound *GdTe* possesses a rocksalt (*NaCl*) structure ($Fm\bar{3}m$) similar to $Ge_2Sb_2Te_5$ with a lattice constant of 6.13 Å[20] close to that of $Ge_2Sb_2Te_5$ (6.01 Å).[21] Geometrical conformability might provide guidelines for developing new phase change materials with improved qualities. Here, we screen out *Gd* to be a promising dopant to enhance the performances of *GST*. It is a prerequisite to characterize the amorphous (*a*-) and crystalline (*c*-)

[a)]Authors to whom correspondence should be addressed: xdhan@bjut.edu.cn; lixianbin@jlu.edu.cn; and welon5337@126.com

phases to optimize *Gd-GST* quaternary materials for various applications. It is also necessary to carry out studies on the phase transition properties and the roles of *Gd* in these processes.

In this work, we provided a valuable insight into the phase change properties, the microscopic structure, and the bonding mechanism of *Gd* incorporated *GST* through experimental investigations and theoretical calculations.

II. EXPERIMENTAL AND COMPUTATIONAL DETAILS

A. Preparation and characterization

Gd-doped $Ge_2Sb_2Te_5$ (*GGST*) films were grown by the magnetron co-sputtering method using separate pure *Gd* (99.99%) and stoichiometric $Ge_2Sb_2Te_5$ alloy targets. Thin film samples of $(GST)_{1-x}Gd_x$ (x = 0 at. %, 0.30 at. %, 3.14 at. %, 4.00 at. %, 6.14 at. %, and 8.52 at. %) were denoted by *GST*, *GGST* (0.30%), *GGST* (3.14%), *GGST* (4.00%), *GGST* (6.14%), and *GGST* (8.52%). The compositions of these as-deposited films were measured by X-Ray Fluorescence (XRF) [Netherlands, PANalytical, Magix (PW2403)]. 200-nm-thick films were fabricated on Si substrates (covered by a 300 nm thick amorphous SiO_2 layer) for X-ray diffraction (XRD), X-ray photoelectron spectroscopy (XPS), and electrical resistance measurements, while ~20 nm-thick *GGST* (6.14%) film was directly deposited on transmission electron microscope (TEM) grids which were covered by an ultrathin (~5 nm) amorphous carbon film as substrate. The sheet resistance of the as-deposited films as a function of temperature (non-isothermal) was measured by four-point probe in a vacuum chamber. Both the as-deposited and annealed films were examined by XRD using a Bruker D8 advance diffraction system (Cu Kα radiation with λ = 0.15418 nm). The chemical bonding states of *GST* and *GGST* were verified by customized XPS. The high angle annular dark field scanning transmission electron microscopy (HAADF-STEM) and the energy-dispersive X-ray (EDX) mapping were performed on a probe-corrected transmission electron microscope (TEM, FEI Titan G2 equipped with a Super EDX system) at 300 kV. The *GGST* (6.14%) film was annealed at 250 °C for 10 min, with a heating rate of 30 °C/min using an *in situ* TEM thermal holder (Gatan 652 double-tilt heating holder) and then cooled to room temperature (RT) before carrying out the STEM and EDX analyses.

B. Density functional theory calculations

Calculations are based on the density functional theory (DFT) with projected augmented plane waves (PAW)[22] pseudo-potential and Perdew-Burke-Ernzerhof (PBE) exchange-correlation functional,[23] as implemented in the VASP code.[24,25] In the adopted pseudo-potentials, the *Ge* [$4s^24p^2$], *Sb* [$5s^25p^3$], *Te* [$5s^25p^4$], and *Gd* [$5p^66s^25d^1$] electrons are considered as valence electrons. Generally, *Gd* often shows a valence of *+3*, which is the same as that of *Sb*. To maintain the stoichiometry, we build the model by substituting *Sb* atoms in the prototypical $Ge_2Sb_2Te_5$. The initial GGST model is a rocksalt cell with *42 Ge*, *32* Sb, *108* Te, and *12 Gd* atoms, which corresponds to a 6.2 at. % doped *Gd*-GST. The density of the initial model after full relaxation is about 5.97 g/cm^3. Then, the amorphous model was realized by the calculated melt-quench technique. First, by NVT *ab initio molecular dynamics* (AIMD), the initial model is melted at a high temperature of 3000 K for 15 ps to eliminate the initial setup. Then, a 15-ps-NVT AIMD at 1100 K (close to the melting point) is run to get a reasonable liquid phase. Next, the liquid is quenched to 300 K with a rate of 15 K/ps. Finally, the amorphous phase after quenching is further annealed at 300 K for 15 ps. Before calculating the electrical properties, the final amorphous model from AIMD is fully relaxed. The density of the final amorphous model after relaxation is 5.64 g/cm^3. The energy cutoff is 300 eV for AIMD simulation and 350 eV for relaxation and property calculations. The K-points are 1 × 1 × 1 Monkhorst-Pack mesh for AIMD or relaxation and 2 × 2 × 2 Monkhorst-Pack mesh for property calculations. The cut-off distances for CN (coordination number) and BAD (bond angle distribution) are 1.15 times the sum of the covalent radius of two bonded atoms.

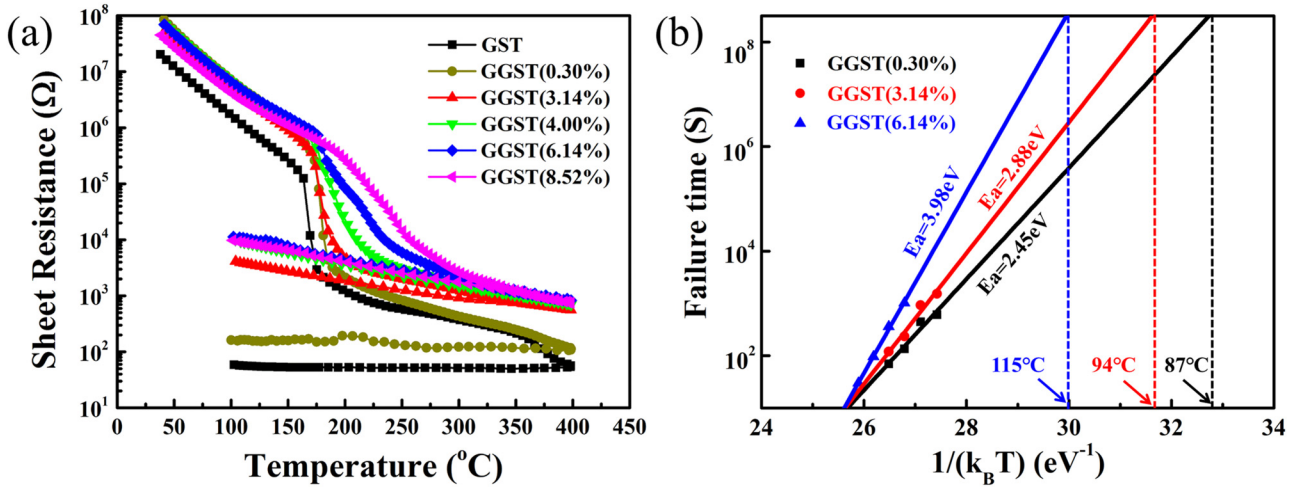

FIG. 1. Temperature-dependence sheet resistance and 10-year retention for *GST* and *GGST* films. (a) Sheet resistance as a function of annealing temperature for *GST* and *GGST* films. (b) The Arrhenius extrapolation for working temperature at 10 years of data retention for *GGST* films with different *Gd* concentrations.

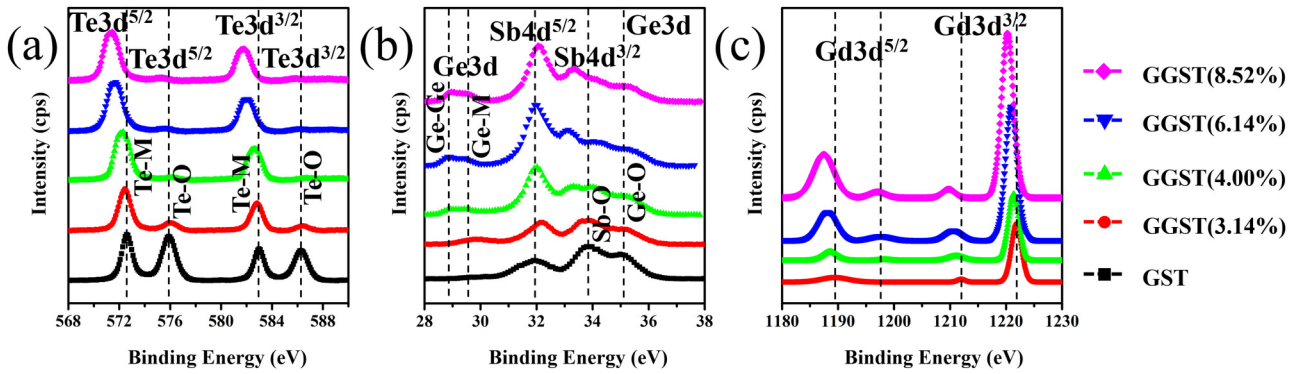

FIG. 2. XPS spectrums for *GST* and *GGST* films. (a) *Te 3d*, (b) *Ge 3d*, *Sb 4d*, (c) *Gd 3d*. Backgrounds were subtracted by the Shirley method.

III. RESULTS AND DISCUSSION

First, the analyses on electrical properties and thermal stability were carried out to characterize the performances of these materials. Figure 1(a) shows the sheet resistance as a function of temperature (R-T) for *GST* and *GGST* films. The initial states of the as-deposited films are amorphous phases [see Fig. 3(a)] with high resistance. In general, the additional *Gd* increases the resistance of the as-deposited samples. In the early stage, the sheet resistance presents a slightly decreasing tendency with the increase of annealing temperature. However, when the temperature reaches a certain value (crystallization temperature T_c, which is determined by a temperature corresponding to the minimum of the first derivative of the R-T curve), the resistance displays a sudden drop to a much lower level, indicating the transition from amorphous to crystalline phases. In addition, the crystalline resistances increase dramatically after doping and exhibit a *Gd*-concentration dependent effect, which is favorable to lower the RESET power consumption for *GGST* based phase change memory. The resistance contrast of 4–5 orders of magnitude between the amorphous and crystalline states of *GGST* is a benefit to achieve a high ON/OFF ratio (signal contrast).[26]

Figure 1(b) shows the thermal stability of amorphous *GGST* (*a-GGST*) films, which can be estimated by calculating the data retention from extrapolation of the isothermal Arrhenius plots according to the Arrhenius equation $t = \tau\ exp\ (E_a/k_BT)$, where t is the failure time, τ is a proportional time coefficient, and E_a is the crystallization activity energy. The failure time is defined as the time when the cell resistance drops to half of its initial value at the specific temperature T. From the slope of lnt versus $1/k_BT$, the values of activation energy for the *GGST* (0.30%), *GGST* (3.14%), and *GGST* (6.14%) films are figured out as 2.45 eV, 2.88 eV, and 3.98 eV, respectively, whereas the E_a of *GST* is only 2.24 eV, and the higher E_a of *GGST* films signifies larger energy barriers that should be overcome to achieve the crystalline states, which indicates that *a-GGST* is more thermally stable than *a-GST*. In addition, the temperature for 10-year data retention of *GGST* (0.30%), *GGST* (3.14%), and *GGST* (6.14%) could also be deduced to be about 87 °C, 94 °C, and 115 °C, respectively. Therefore, Gd doping is an excellent approach for improving the thermal stability of *GST* and is helpful to satisfy the requirements of automotive systems for long-term data storage.

XPS is further applied to investigate the binding states of as-deposited amorphous *GST* and *GGST*. The core level spectra of *Te 3d*, *Ge 3d*, *Sb 4d*, and *Gd 3d* are shown for the amorphous phases in Fig. 2. Surface charge compensation and spectral calibration were achieved by assigning a binding energy (BE) of 284.8 eV to the adventitious carbon *1s* photoelectron line. As illustrated in Fig. 2(a), the peaks of *Te–O* (~575.9 eV and ~586.3 eV) appear in *GST* but vanished

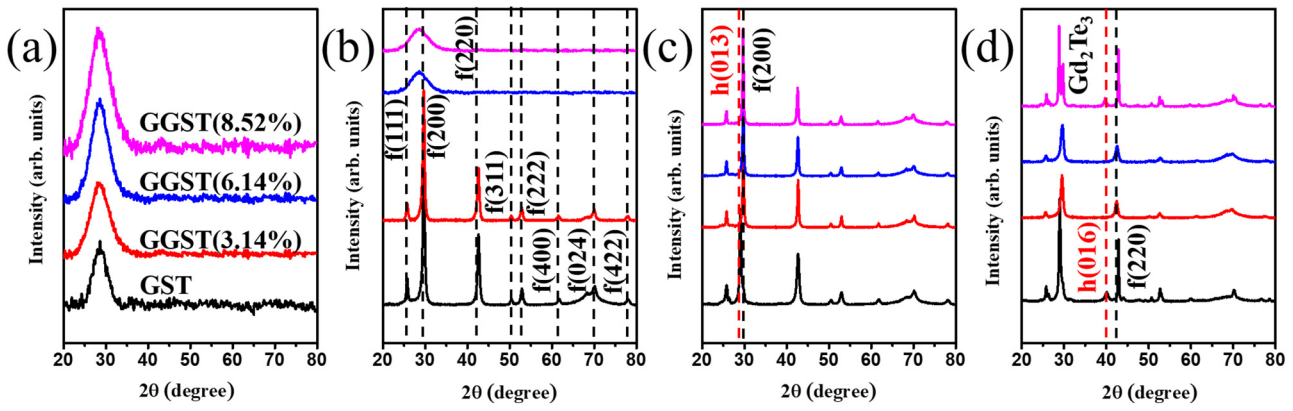

FIG. 3. XRD patterns for *GST* and *GGST* films. (a) XRD for as-deposited films and after 10-min-annealing at (b) 200 °C, (c) 250 °C, and (d) 300 °C, respectively. The vertical black and red dotted lines indicate the cubic and hexagonal phases, respectively. The secondary phase Gd_2Te_3 occurs when the dopants increase to 8.52 at. % at 300 °C.

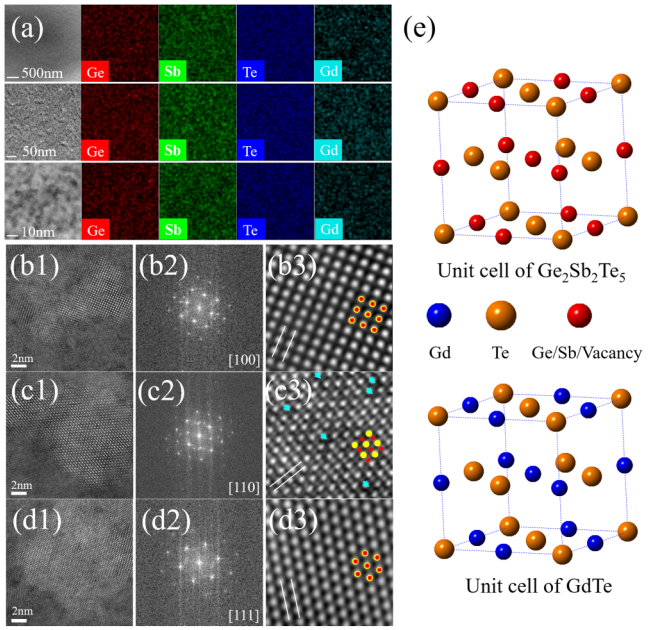

FIG. 4. Chemical and structural identifications of *GGST* (6.14%) by TEM. (a) HAADF-STEM images and the corresponding individual EDX mappings of *Ge*, *Sb*, *Te* and *Gd*, respectively. [(b1)–(d1)] HAADF-STEM images, [(b2)–(d2)] the corresponding FFT patterns of the 250 °C-annealed (for 10 min) film, [(b3)–(d3)] the enlarged HAADF-STEM images with atomic resolution. The lattice spacing [guided by the white lines in (b3)–(d3)] are 3.00 Å (200), 2.14 Å (220), and 2.14 Å (220), respectively. The atomic arrangements are depicted by the colored spheres, and the arrows indicate the vacancies of *GGST* in (c3). (e) The schematics of *GST* and *GdTe* atomic structures.

after *Gd* doping, indicating that the *Gd* dopants can significantly prevent oxidation. The binding energy of *Te 3d* shifts toward the lower direction as *Gd* dopants increasing, which suggests that *Gd–Te* bond could be formed. Previous results demonstrated that vacancies and voids, which are surrounded by *Te* atoms in amorphous *GST*, play important roles in fast reversible phase transition process.[27] It is reasonable that *Gd* changes the local structures around *Te* due to its relatively small electronegativity and large atomic size; thus, *Gd* dopants disturb the crystallization behaviors of pristine *GST*.

Figure 2(b) displays the XPS spectra of the *Ge 3d* and *Sb 4d*. No peaks at 29–30 eV (related to the *Ge–Ge* homopolar bonds)[28] are present in sputtered amorphous *GST*, while the *Ge–O* peak (at ~35 eV) is easily discernible. Notably, the *Ge–Ge* and *Ge–M* (metal) peaks are apparent in *GGSTs* and gradually become stronger as the *Gd* concentration increases, concomitant with the weakening of *Ge–O* peaks, which once again indicates that oxidation is suppressed after *Gd* doping. It is also noteworthy that *Sb 4d* levels show noticeable change as *Gd* dopants increase, displaying variations of local structures around *Sb*.

In Fig. 2(c), the *Gd 3d* signals are dominated by the two main spin orbit components *Gd 3d5/2* and *Gd 3d3/2*, in good agreement with some other *Gd*-containing compounds.[29] Basically, in *GGST* samples, the XPS spectra of *Gd* seem to be similar, while the binding energies and full width half maximum (FWHM) are quite different. The binding energies of *Gd* are higher than that of *Gd* pure metal,[30] which indicate that they (in *GGST*) are no longer related to metallic bonds (*Gd–Gd*). With increasing of *Gd* content, the intensities of the *Gd 3d5/2* peaks increase gradually. The *Gd 3d5/2* main peak position shifts from 1189.4 eV to 1187.5 eV, and the *Gd 3d3/2* signal shifts from 1221.9 eV to 1220.3 eV. The value of the exchange splitting is 32.8 eV for the 3d level. Clear chemical shifts can be owed to the change of *Gd* chemical environment. In addition, two weak satellites that entered between the main *Gd 3d5/2* and *Gd 3d3/2* components could be observed, which are very different from that of *Gd* metal.[30] Energy-loss phenomena are suggested to be the possible effects for the satellites peaks.[31]

Figure 3 shows the XRD patterns of the *GST* and *GGST* films with various doping levels and annealing temperatures. No characteristic peaks are observed in Fig. 3(a), which indicates the amorphous nature of the as-deposited films. Some diffraction peaks corresponding to the cubic rocksalt structure (RS) phase appear in the *GST* film and *GGST* (3.14%) after annealing at 200 °C as shown in Fig. 3(b). However, *GGST* (6.14%) and *GGST* (8.52%) films (annealed at 200 °C) remain amorphous phase, which are consistent with the results of R-T in Fig. 1(a). It can be concluded that the

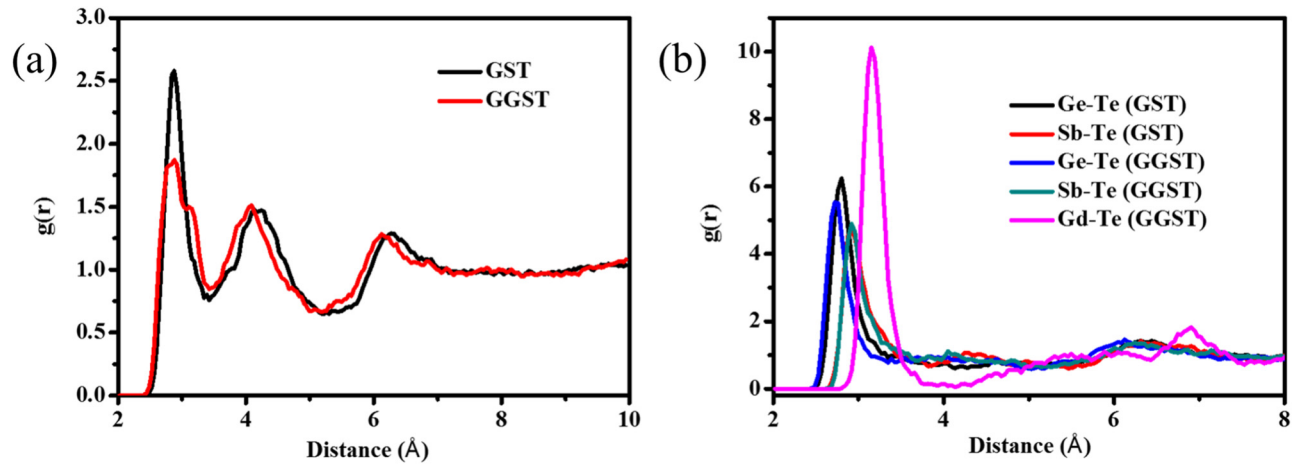

FIG. 5. Pair correlation function (PCF) of amorphous *GST* and *GGST* (6.2 at. %). (a) The total PCFs of amorphous *GST* and *GGST*. (b) The partial PCFs for various atomic connections.

TABLE I. The partial coordination numbers (CN) of a-GST and a-GGST.

	N_{Ge}	N_{Sb}	N_{Te}	N_{Gd}	Total
GST	3.03	3.45	2.40	…	2.77
GGST	3.29	3.55	2.78	7.25	3.31

crystallization process of *GST* is delayed by *Gd* doping. Thus, the increase of T_c suggests the improved thermal stability and will contribute to enhance the data retention for phase change memories. In Fig. 3(c), the peaks of hexagonal (HEX) phase in *GST* annealed at 250 °C are formed. However, the RS phases are observed in *GGST* (3.14%), *GGST* (6.14%), and *GGST* (8.52%) at the same annealing temperature. Figure 3(d) shows that the undoped *GST* film is dominated by HEX phase at 300 °C, while the *GGST* (3.14%) and *GGST* (6.14%) films still maintain as RS phase. Thus, the transition process from RS to HEX phase is suppressed by the *Gd* doping. By further increase of doping level to 8.52%, the phase segregation of Gd_2Te_3 occurs. In the practice, phase separations will cause device failure, so the appropriate concentration of dopant for *GGST* is necessary for the reliability of PCM devices.

Figure 4 shows the chemical and structural identifications of *GGST* (6.14%) film annealed at 250 °C for 10 min by TEM analysis. The elemental mappings within the scope of different scales in Fig. 4(a) demonstrate the presence of *Gd*, *Ge*, *Sb,* and *Te* elements with uniformly spatial distributions, which are beneficial to data retention. Furthermore, the HAADF-STEM images display the atomic arrangements along the [100], [110], and [111] directions, as displayed in Figs. 4(b) and 4(c). Both the STEM images and the corresponding fast Fourier transformation (FFT) patterns confirm the cubic crystal structure of *GGST*. Figures 4(b3)–4(d3) show the enlarged HAADF-STEM images with atomic resolution, and the corresponding atomic arrangements are depicted by spheres in the right hand side. Each atomic column along the [100] and [111] directions is uniformly constituted of all these three elements, while the cation and anion atoms reside on different sublattices along the [110] direction. The brightness of the spots appears to be rather uniform in Figs. 4(b3) and 4(d3), in contrast to the two distinguishable sublattices in Fig. 4(c3). The white lines show that the lattice spacing of (200) and (220) planes are 3.00 Å [Fig. 4(b3)] and 2.14 Å [Figs. 4(c3) and 4(d3)], respectively, which are similar to those of *GST*.[32–34] No obvious distortion is presented in the crystalline structure, which implies that *Gd* distributes uniformly and may replace the original cations lattice in the *GST* cubic structure. Normally, vacancies would have ordering effects in *GST* during the transition from the RS to the HEX structure.[32,35,36] However, the vacancies still randomly distribute in *GGST* [Fig. 4(c3)] rather than being ordered onto specific (111) planes in *GST*.[32,36] Figure 4(e) shows the atomic structure of the $Ge_2Sb_2Te_5$ and *GdTe*, where both have a RS structure ($Fm\bar{3}m$) with close lattice constants (as discussed before). This should be the main reason for the single cubic phase after suitable doping. Obviously, the geometrical conformability and the small lattice mismatch (~2%) would contribute positive impacts on the SET and RESET processes. As a result, *Gd* doping effectively inhibits the structure transition from RS phase to HEX phase, in contrast to the case of *GST*.[32]

To further comprehend the origin of the high thermal stability of *a-GGST*, we investigated the detailed bonding mechanism by first-principles calculations based on the density functional theory (DFT) with projected augmented plane waves (PAW) pseudopotential[22] and Perdew-Burke-Ernzerhof (PBE) exchange-correlation functional,[23] as implemented in the VASP code.[24,25] The model of *a-GST* is obtained by the melt-quench technique, see the details of Sec. II B. The pair correlation function (PCF) is a useful structure analysis method for the local structure of amorphous states.[37,38] Figure 5 shows the total [Fig. 5(a)] and partial [Fig. 5(b)] atomic pair correlations of *a-GST* and *a-GGST*. The convergence of the PCFs to *1* at large distance demonstrates the disorder of the present models. A shoulder peak at about 3.1 Å in the total PCF of *a-GGST* compared with that of *a-GST* clearly displays the

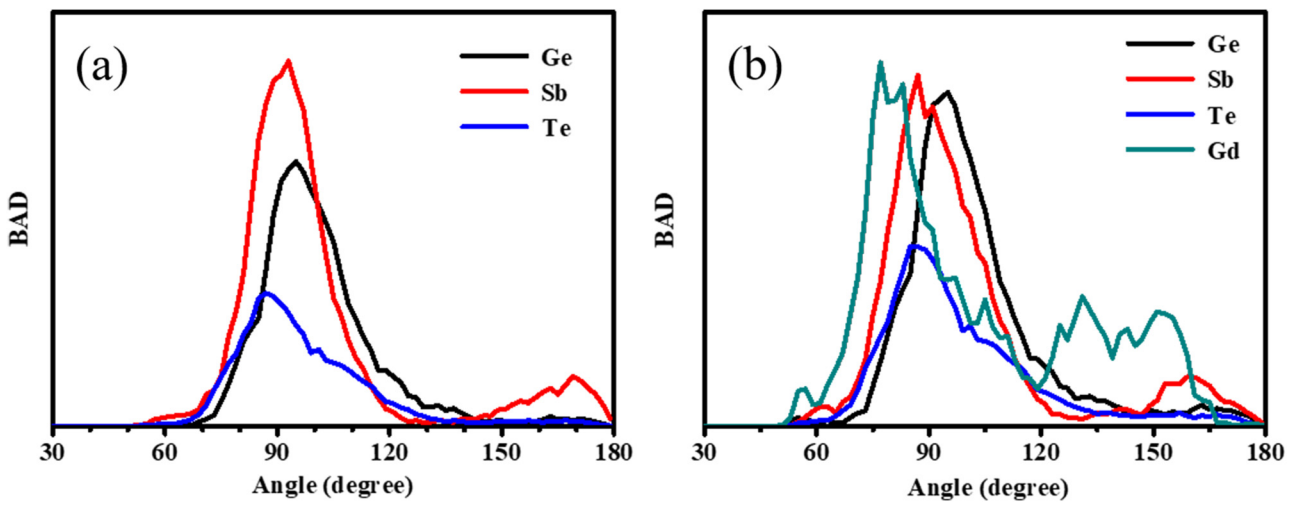

FIG. 6. The bond angle distributions (BADs) in *a-GST* and *a-GGST*. (a) The partial BADs in *a-GST* around *Ge*, *Sb*, and *Te*, respectively. (b) The partial BADs in *a-GGST* around *Ge*, *Sb*, *Te*, and *Gd*, respectively.

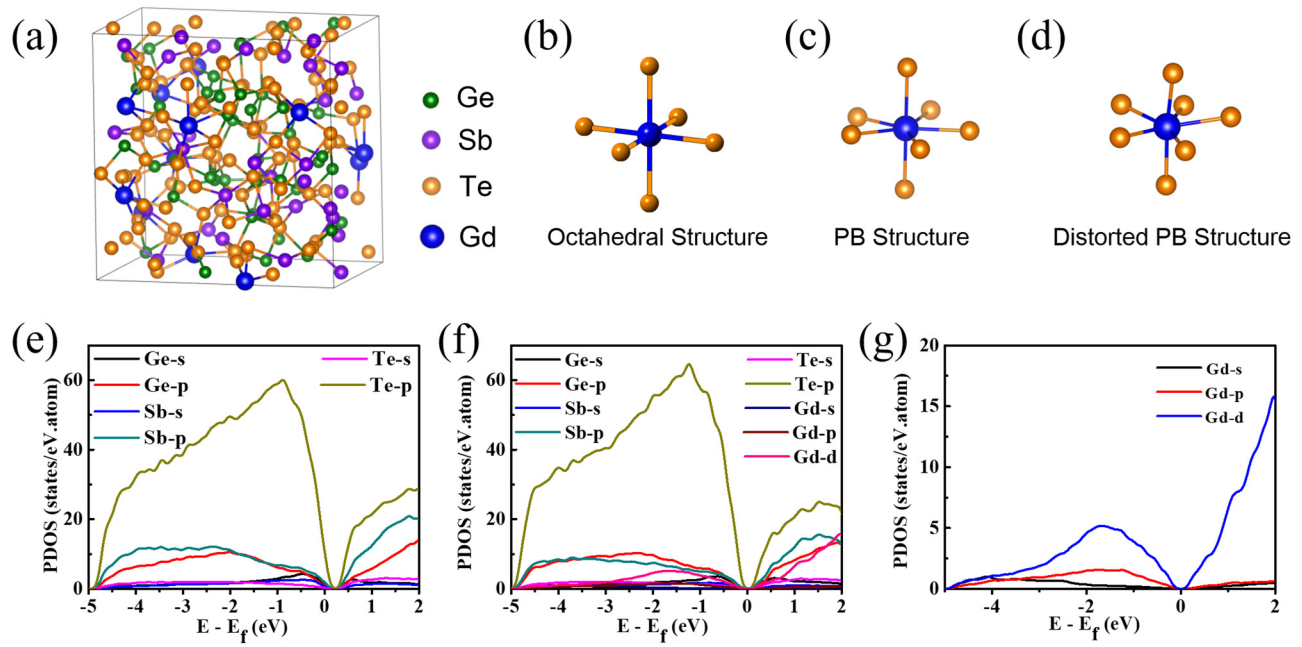

FIG. 7. Structural snapshots and the partial density of states (PDOS) of *a-GST* and *a-GGST*. (a) A structural model of *a-GGST*. [(b)–(d)] The schematics of the *Gd*-centered local motifs of octahedral atomic structure (b) in *c-GdTe*, the pentagonal bipyramidal (c), the distorted pentagonal bipyramidal atomic structure (d) of *a-GGST*. [(e) and (f)] The PDOS of *a-GST* and *a-GGST*, respectively. (g) The PDOS of *Gd* element in *a-GGST*.

different bonding tendency. In Table I, the average coordination number (CN) for all elements of *a-GGST* is 3.31, which is larger than that of *a-GST* (2.77) at the same condition of bond-length cutoff. The CNs of each element in *a-GGST* display an increasing tendency compared with those of *a-GST*. Notably, *Gd* has a max CN of 7.25, far beyond the CNs of *Ge*, *Sb*, and *Te*. The high CN of *Gd* may result from its especially low electronegativity as easy to form *Cd–Te* bonds. Figure S1 in the supplementary material shows all the atomic pair correlations and reveals a very strong *Gd–Te* bonding tendency but a relatively weak *Gd–Gd* bonding tendency.

Bond angle distributions (BADs) are also useful to detect the local structure features.[37] Generally, a 90° angle often implies a *p*-bonding octahedral motif which is very popular in PCMs, such as the case of *GST* [Fig. 6(a)].[39] It is noted that *Ge*, *Sb*, and *Te* have broad BAD peaks at 95°, 87°, and 85° in *a-GGST* [Fig. 6(b)], respectively, which are close to those of *a-GST* as shown in Fig. 6(a). In general, *a-GGST* keeps the main octahedral local environment just as *a-GST* does. However, there is a striking contrast by an obvious BAD peak of *Gd* at about 77°, indicating a *Gd*-related *Gd–Te* bonding environment. From CNs, BADs, and strong bonding tendency of *Gd* (with *Te*) in *a-GGST*, the *Gd*-centered atomic motifs are shown in Fig. 7. Figure 7(a) displays an amorphous structure model of *GGST*. Instead of the standard octahedral motif in the cubic *GdTe* compound [Fig. 7(b)], the atoms are arranged with BADs of 72° and 90° in the normal pentagonal bipyramidal (PB) atomic model in Fig. 7(c). The *Gd–Te* local motif in *a-GGST* can be viewed as a severe distortion in PB-type model with 77° bond angles displayed in Fig. 7(d). This (the distorted PB-like structure) is the most distinct local structures for *a-GGST* compared to those of *a-GST*, thereby resulting in a high thermal stability of *a-GGST*. Meanwhile, the normal octahedral motif and the distorted PB-like structure are similar to some extent, which should benefit the phase change process. In fact, the increase in total average CN suggests that more electrons are required in *a-GGST* for bonding compared to that of *a-GST*, especially for the *Gd–Te* distorted PB-like structure. There are only two electrons in *6s* shell and one electron in *5d* shell of *Gd*, yet the CN is beyond 7. Here, the atomic orbital hybridization should occur to make up for the lack of electrons. The partial density of states (PDOS) of *a-GST* and *a-GGST* are shown in Figs. 7(e) and 7(f), respectively. The distributions of *d* and *p* electrons in *a-GGST* in PDOS [Fig. 7(g)] indicate that they are involved in the bonding (which is also exited in *GGST* crystalline model; see Fig. S2 of the supplementary material). The sp^3d^3-like hybridization is a possible explanation for the *Gd–Te* distorted PB-like structure.[40,41]

IV. CONCLUSION

In summary, the electrical properties, crystallization behaviors, and structure of the *GGST* films were studied systematically. The higher crystallization temperature, activation energy, and better 10-year data-retention temperature elucidate the improved thermal stability of the *Gd* doped *GST* alloys. The dramatically increased crystalline resistance is favorable to lower the RESET power consumption for *GGST* based phase change memory. In the amorphous state, *Gd* dopants change the local structures and disturb the crystallization behaviors through suppressing the transition from RS phase to HEX phase, which could be helpful to improve the data retention performance. The EDX mappings and HAADF-STEM observations demonstrate the homogeneous distribution of all elements in *GGST* films. No obvious distortion of crystal structure after the *Gd* doping occurs and

vacancies are also randomly distributed. These properties are mainly owing to the geometrical conformability and less lattice mismatch between *GST* and *GdTe*. The AIMD calculations reveal the detailed bonding mechanism in *a-GGST* that *Gd*-centered sp^3d^3-like hybridization results in a large coordination for *Gd*, possibly in the form of distorted pentagonal bipyramidal structures. The present phase-change material incorporated with rare-earth element *Gd* should be applicable in non-volatile memory, especially for high-data retention and low-power consumption applications.[42]

SUPPLEMENTARY MATERIAL

Both the pair correlation function (PCF) of amorphous *GST* and *GGST* (6%) for every kind of atomic connection and the partial density of states (PDOS) of crystalline *GGST* (6%) are available in the supplementary material.

ACKNOWLEDGMENTS

X. D. Han thanks the support from National Key R&D Program of China (No. 2017YFB0305501) and National Natural Science Foundation of China (NSFC) (Grants Nos. 11327901 and 51471008). X. B. Li acknowledges the support from the National Natural Science Foundation of China (NSFC) (Grants Nos. 11874171 and 61775077). B. Zhang thanks the Fundamental Research Funds for the Central Universities of China (Grant No. 0903005203553).

[1]D. Loke, T. H. Lee, W. J. Wang, L. P. Shi, R. Zhao, Y. C. Yeo, T. C. Chong, and S. R. Elliott, Science **336**, 1566 (2012).
[2]C. Ríos, M. Stegmaier, P. Hosseini, D. Wang, T. Scherer, C. D. Wright, H. Bhaskaran, and W. H. P. Pernice, Nat. Photon. **9**, 725 (2015).
[3]C. D. Wright, Y. Liu, K. I. Kohary, M. M. Aziz, and R. J. Hicken, Adv. Mater. **23**, 3408 (2011).
[4]P. Hosseini, C. D. Wright, and H. Bhaskaran, Nature **511**, 206 (2014).
[5]M. Cassinerio, N. Ciocchini, and D. Ielmini, Adv. Mater. **25**, 5975 (2013).
[6]K. Wang, C. Steitner, D. Warnwangi, S. Ziegler, M. Wuttig, J. Tomforde, and W. Bensch, Microsyst. Technol. **13**, 203 (2007).
[7]W. D. Song, L. P. Shi, X. S. Miao, and C. T. Chong, Adv. Mater. **20**, 2394 (2008).
[8]K. B. Borisenko, Y. Chen, D. J. H. Cockayne, S. A. Song, and H. S. Jeong, Acta Mater. **59**, 4335 (2011).
[9]S. J. Wei, H. F. Zhu, K. Chen, D. Xu, J. Li, F. X. Gan, X. Zhang, Y. J. Xia, and G. H. Li, Appl. Phys. Lett. **98**, 231910 (2011).
[10]Y. J. Huang, M. C. Tsai, C. H. Wang, and T. E. Hsieh, Thin Solid Films **520**, 3692 (2012).
[11]L. Tong, L. Xu, Y. Jiang, F. Yang, L. Geng, J. Xu, W. Su, Z. Ma, and K. Chen, J. Non-Cryst. Solids **358**, 2402 (2012).
[12]B. Prasai, M. E. Kordesch, D. A. Drabold, and G. Chen, Phys. Status Solidi B **250**, 1785 (2013).
[13]T. Zhang, B. Zhang, R. Shao, and K. Zheng, Mater. Lett. **128**, 329 (2014).
[14]E. M. Vinod, K. Ramesh, and K. S. Sangunni, Sci. Rep. **5**, 8050 (2015).
[15]Z. Li, Y. Lu, Y. Ma, S. Song, X. Shen, G. Wang, S. Dai, and Z. Song, J. Non-Cryst. Solids **452**, 9 (2016).
[16]F. Rao, K. Ding, Y. Zhou, Y. Zheng, M. Xia, S. Lv, S. Zhitang, S. L. Feng, I. Ronneberger, R. Mazzarello, W. Zhang, and E. Ma, Science **358**, 1423 (2017).
[17]H. Zou, L. Zhai, Y. Hu, X. Zhu, H. You, J. Zhang, S. Song, and Z. Song, RSC Adv. **7**, 56000 (2017).
[18]Z. Li, C. Si, J. Zhou, H. B. Xu, and Z. M. Sun, ACS Appl. Mater. Interfaces **8**, 26126 (2016).
[19]Z. Li, N. Miao, J. Zhou, H. Xu, and Z. Sun, J. Appl. Phys. **122**, 195107 (2017).
[20]P. Villars and L. D. Calvert, *Pearson's Handbook of Crystallographic Data for Intermetallic Phases*, 2nd ed. (ASM International, Materials Park, 1991).
[21]T. Nonaka, G. Ohbayashi, Y. Toriumi, Y. Mori, and H. Hashimoto, Thin Solid Films **370**, 258 (2000).
[22]G. Kresse and D. Joubert, Phys. Rev. B **59**, 1758 (1999).
[23]J. P. Perdew, K. Burke, and M. Ernzerhof, Phys. Rev. Lett. **77**, 3865 (1996).
[24]G. Kresse and J. Furthmüller, Phys. Rev. B **54**, 11169 (1996).
[25]G. Kresse and J. Furthmüller, Comput. Mater. Sci. **6**, 15 (1996).
[26]C. Wang, S. Li, J. Zhai, B. Shen, M. Sun, and T. Lai, Scripta Mater. **64**, 645 (2011).
[27]Z. Sun, J. Zhou, A. Blomqvist, B. Johansson, and R. Ahuja, Phys. Rev. Lett. **102**, 075504 (2009).
[28]B. V. Crist, *Handbook of Monochromatic XPS Spectra* (John Wiley & Sons, Chichester, 1999).
[29]D. Raiser and J. P. Deville, J. Electron Spectrosc. Relat. Phenom. **57**, 91 (1991).
[30]M. Neumann and J. Szade, J. Phys. Condens. Matter **13**, 2717 (2001).
[31]D. Barreca, A. Gasparotto, A. Milanov, E. Tondello, A. Devi, and R. A. Fischer, Surf. Sci. Spectra **14**, 60 (2007).
[32]B. Zhang, W. Zhang, Z. Shen, Y. Chen, J. Li, S. Zhang, Z. Zhang, M. Wuttig, R. Mazzarello, E. Ma, and X. Han, Appl. Phys. Lett. **108**, 191902 (2016).
[33]T. Matsunaga and N. Yamada, Phys. Rev. B **69**, 104111 (2004).
[34]N. Yamada and T. Matsunaga, J. Appl. Phys. **88**, 7020 (2000).
[35]T. Siegrist, P. Jost, H. Volker, M. Woda, P. Merkelbach, C. Schlockermann, and M. Wuttig, Nat. Mater. **10**, 202 (2011).
[36]W. Zhang, A. Thiess, P. Zalden, R. Zeller, P. H. Dederichs, J. Y. Raty, M. Wuttig, S. Blügel, and R. Mazzarello, Nat. Mater. **11**, 952 (2012).
[37]X. B. Li, X. Q. Liu, X. Liu, D. Han, Z. Zhang, X. D. Han, H. B. Sun, and S. B. Zhang, Phys. Rev. Lett. **107**, 015501 (2011).
[38]N. K. Chen, X. B. Li, X. P. Wang, M. J. Xia, S. Y. Xie, H. Y. Wang, Z. Song, S. Zhang, and H. B. Sun, Acta Mater. **90**, 88 (2015).
[39]J. Hegedüs and S. R. Elliott, Nat. Mater. **7**, 399 (2008).
[40]B. Douglas, D. McDaniel, and J. Alexander, *Concepts and Models of Inorganic Chemistry*, 3rd ed. (John Wiley & Sons, New York, 1994).
[41]A. Das, IOSR, J. Appl. Chem. **6**, 8 (2013).
[42]X. B. Li, N. K. Chen, X. P. Wang, and H. B. Sun, "Phase-change superlattice materials toward low power consumption and high density data storage: Microscopic picture, working principles, and optimization," Adv. Funct. Mater. 1803380 (published online).